Journal of Magnetic Resonance 205 (2010) 293–303

Contents lists available at ScienceDirect

Journal of Magnetic Resonance

journal homepage: www.elsevier.com/locate/jmr

Electronic structure and dynamics of low symmetry Cu^{2+} complexes in kainite-type crystal $KZnClSO_4{\cdot}3H_2O$: EPR and ESE studies

Stanisław K. Hoffmann *, Janina Goslar, Krzysztof Tadyszak

Institute of Molecular Physics, Polish Academy of Sciences, PL-60179 Poznań, Poland

ARTICLE INFO

Article history:
Received 23 March 2010
Revised 19 May 2010
Available online 26 May 2010

Keywords:
EPR of Cu^{2+}
Jahn–Teller effect
Motional averaging
Electron spin echo
Electron spin relaxation

ABSTRACT

EPR measurements at X-band were performed in the temperature range 4.2–300 K with angular dependence measurements at 77 K for Cu^{2+} in $KZnClSO_4{\cdot}3H_2O$. Rigid lattice spin – Hamiltonian parameters are: $g_z = 2.4247$, $g_y = 2.0331$, $g_x = 2.1535$, $A_z = -103 \times 10^{-4}\,cm^{-1}$, $63 \times 10^{-4}\,cm^{-1}$, and $-31 \times 10^{-4}\,cm^{-1}$. The parameters were analyzed using MO-theory with the $d_{x^2-y^2}$ ground state containing admixture of the d_{z^2}-state in the rhombic symmetry D_{2h}. The analysis consistently explained unusual *g*-factor sequence and relatively small hyperfine splitting anisotropy as the consequence of the mixing and spin density delocalization *via* excited orbital states. We assigned that Cu^{2+} ions substituting host Zn^{2+} prefer one of the four structurally different zinc sites where they are coordinated by four water molecules and two SO_4 groups in an distorted octahedron elongated along SO_4–Cu–SO_4 direction. The distortion is due to the Jahn–Teller effect which is static at low temperatures but becomes dynamic above 20 K with jumps of the Cu^{2+} complex between two lowest potential wells. The jumps produce continuous *g*-factor and hyperfine splitting averaging when temperature increases. This process is discussed in terms of two motional averaging theories: classical theory based on generalized Bloch equations and Silver–Getz model. Their limitations are discussed. Importance of the difference in the *g*-factors of the averaged line is explained and a new expression for calculation of jump frequency from the line shift is proposed. The jumps are described as phonon induced tunneling *via* excited vibrational level of energy 76 (±6) cm^{-1}. This process is not effective enough at low temperatures and Boltzmann population of the two lowest energy potential wells is reached above 110 K. From electron spin–lattice relaxation measurements by electron spin echo methods the Debye temperature was determined as $\Theta_D = 172$ K. Fourier Transform of strongly modulated spin echo decay gives pseudo-ENDOR spectrum with peaks from ^1H and ^{35}Cl nuclei. From splitting of the peaks into doublets we determined the distance to the modulating nuclei and confirmed the position of the site where Cu^{2+} ion is located.

1. Introduction

Kainite, $KMgClSO_4{\cdot}3H_2O$, is a well known sedimentary mineral used in fertilizer industry. Various divalent and trivalent paramagnetic ions have been introduced into the host lattice and studied by spectroscopic methods [1–6]. Some of the ions form photoluminescence centers [7]. Isomorphous crystals $KZnClSO_4{\cdot}3H_2O$ have also been doped and studied by optical, IR and EPR methods [8–10]. Characteristic feature of kainite crystals is an existence of four different types of Mg^{2+} coordination to surrounding oxygen atoms with $Z = 16$ in monoclinic unit cell. The divalent guest ions substitute Mg^{2+} host ions, but it is open to question which sites are occupied. EPR studies of Cu^{2+} in kainite [5,6] and its Zn-analogue [9,10] have not provided an answer to this question. Because of a low accuracy of angular EPR measurements the two identical symmetry related Cu^{2+} sites were treated as two distinct centers [5,6,10] and in angular variations of EPR spectra the twofold symmetry *b*-axis has been incorrectly assigned [6,10]. Moreover, in the discussion of the results an apparent domination of the d_{z^2} has been assumed although in [5] the correct $g_z > g_x$ sequence characteristic for $d_{x^2-y^2}$ has been chosen. It should be noted, that the EPR parameter values are very similar in kainite and its Zn-analogue, but display large *g*-factor anisotropy and unusually small hyperfine splitting anisotropy in contrast to most of Cu^{2+} complexes. In the published papers the strong temperature dependence of EPR spectra has been presented with the suggestion that it is due to the Jahn–Teller effect. This has not been discussed qualitatively and raw experimental data has been presented only.

In this paper we verify the previous EPR measurements. On the basis of angular dependence measurements in two reference frames and making the Fourier Transform of modulated electron spin echo spectra we have identified the sites which are preferred

* Corresponding author. Address: Institute of Molecular Physics, Polish Academy of Science, Smoluchowskiego 17, 60-179 Poznań, Poland. Fax: +48 61 8684 524.
E-mail address: skh@ifmpan.poznan.pl (S.K. Hoffmann).

1090-7807/$ - see front matter © 2010 Elsevier Inc. All rights reserved.
doi:10.1016/j.jmr.2010.05.014

for occupation by Cu^{2+} ions. Detailed analysis of spin-Hamiltonian in terms of MO-theory for low crystal field symmetry allowed us to determine the ground state with parameters consistent with existing optical absorption spectra and explain rather untypical EPR parameters. We performed quantitative analysis of temperature dependence of the spectra resulting from reorientations of Cu^{2+} between two non-equivalent potential wells. We applied two theories for description of the reorientation dynamics. We show that an analysis of motional averaging of the lines having different *g*-factors is more complex than that usually used for free radicals. A new expression for calculation of the reorientation rate from the line shift is proposed.

2. Crystal structure

For the discussion of EPR and ESE measurements results we have to refer to the details of the crystal structure. Kainite is a monoclinic crystal with space group C2/m and with the unit cell dimensions: $a = 1.972$ nm, $b = 1.623$ nm, $c = 0.953$ nm, $\beta = 94.92°$, and $Z = 16$ [11]. The crystal structure of $KZnClSO_4{\cdot}3H_2O$ is not known and we assume isomorphous structure of kainite and its Zn-analogue in which magnesium ions are replaced by zinc ions. The projection of the structure on the *ab*-plane is shown in Fig. 1. Thus, the crystal structure of $KZnClSO_4{\cdot}3H_2O$ is built with corner shared ZnO_6-octahedra and SO_4-tetrahedra. They are arranged in layers parallel to the (1 0 0) plane which is a cleavage crystal plane. K^+, Cl^-, and H_2O molecules are located in the interlayer space. All oxygen atoms of the sulfate groups are involved in coordination bonds to the Zn^{2+} ions, whereas the water molecules can form hydrogen bonds with neighboring chlorine atoms.

The hydrogen atom positions have not been determined, but the short hydrogen bonds to the Zn-coordinated water molecules can be responsible for a slightly irregular octahedral symmetry. The possible hydrogen bonds with O—Cl length lower than 0.4 nm we have calculated from structural data around one of the ZnO_6 octahedron. These bonds are shown by dashed lines in Fig. 2 and its length is given in Table 1. An asymmetry in hydrogen bonding of the water oxygens W_3 and W_6 should be noted. The W_3 oxygen atoms are connected by two short bonds to the two Cl_3 atoms, whereas W_6 oxygen atoms are weakly bonded to Cl_1 and Cl_3 atoms. The clear asymmetry in positions of the nearest Cl_3^{86} and Cl_3^{89} atoms with respect to the Zn–O directions will influence markedly the spin delocalization and EPR parameters as it will be discussed below.

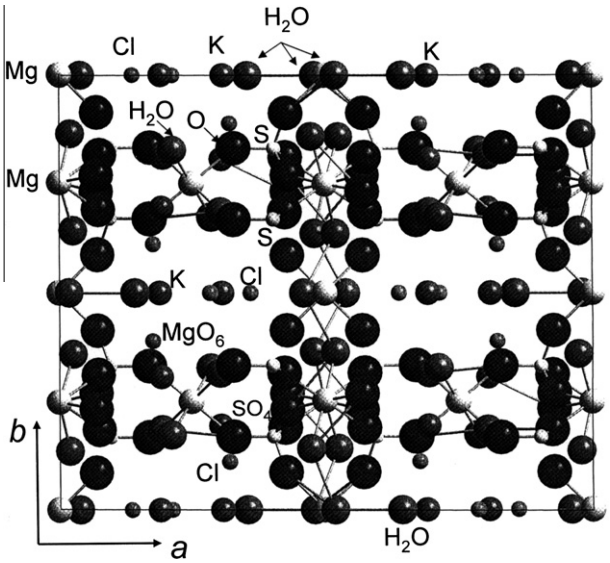

Fig. 1. Kainite $KMgClSO_4{\cdot}3H_2O$ ($Z = 16$) unit cell projection on the *ab*-plane.

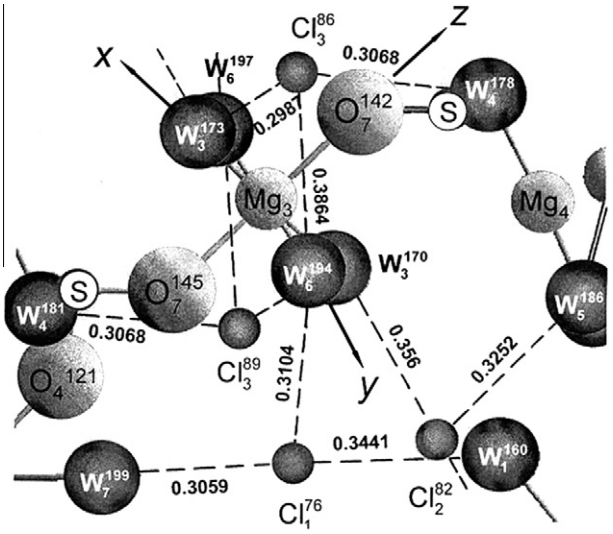

Fig. 2. Hydrogen Cl—H_2O bond network showing asymmetry in bond length and chlorine atom position around Zn_3 octahedron. Water oxygen is marked as W. The numbering of the atoms is consistent with Table of created atoms by Diamond Database code 9000282. The *x*, *y*, and *z* are principal axes of the local crystal field according to the EPR measurements.

Table 1
Length of the possible Cl—O_{water} hydrogen bonds in kainite around the Zn_3 complex.

Water oxygen atom		Chlorine atom		Distance (nm)
Atom No.	Coordinate	Atom No.	Coordinate	
W_3^{173}	$x, 1-y, z$	Cl_3^{86}	$0.5-x, 0.5+y, 1-z$	0.29865
W_3^{170}	$0.5-x, 0.5+y, 1-z$	Cl_3^{89}	$x, 1-y, z$	0.3864
W_6^{194}	$0.5-x, 0.5+y, 1-z$	Cl_3^{86}	$0.5-x, 0.5+y, 1-z$	0.3864
W_6^{197}	$x, 1-y, z$	Cl_3^{89}	$x, 1-y, z$	0.29865
W_3^{170}	$0.5-x, 0.5+y, 1-z$	Cl_2^{82}	$0.5-x, 0.5+y, 1-z$	0.31558
W_6^{194}	$0.5-x, 0.5+y, 1-z$	Cl_1^{76}	$0.5-x, 0.5+y, 1-z$	0.31039
W_1^{160}	$0.5-x, 0.5+y, 1-z$	Cl_1^{76}	$0.5-x, 0.5+y, 1-z$	0.34409
W_4^{181}	$x, 1-y, z$	Cl_3^{89}	$x, 1-y, z$	0.3068
W_5^{186}	$0.5-x, 0.5+y, 1-z$	Cl_2^{82}	$0.5-x, 0.5+y, 1-z$	0.3252
W_7^{199}	x, y, z	Cl_1^{76}	$0.5-x, 0.5+y, 1-z$	0.30588

Four geometrically different types of weakly elongated ZnO_6-octahedra exist in the crystal unit cell each with four symmetry related units (Fig. 1). They are marked as Zn_1, Zn_2, Zn_3, and Zn_4 in Fig. 3. The Zn_1, Zn_2, and Zn_4 are coordinated by four oxygens of different sulfate groups and by two water molecules and are located within the layers, whereas the Zn_3 is coordinated by two sulfate oxygens and four water molecules, and occupies interlayer site. Different orientations of the in-plane and elongation metal–ligand axes in the different types of the octahedra, clearly visible in Fig. 3, allow determination the doped Cu^{2+}-ion site from analysis of the angular dependence of EPR spectra.

3. Experimental

Single crystals of $KZnClSO_4{\cdot}3H_2O$ were grown by slow evaporation of the water solution of equimolar ratio of KCl and $ZnSO_4{\cdot}7H_2O$ with small amount (about 0.1 wt.%) of copper sulfate pentahydrate. Cu^{2+} ion concentration was 2×10^{18} ions $gram^{-1}$ as determined from integral intensity of EPR spectrum. Crystals exhibit various forms depending on the details of growing conditions. Slow

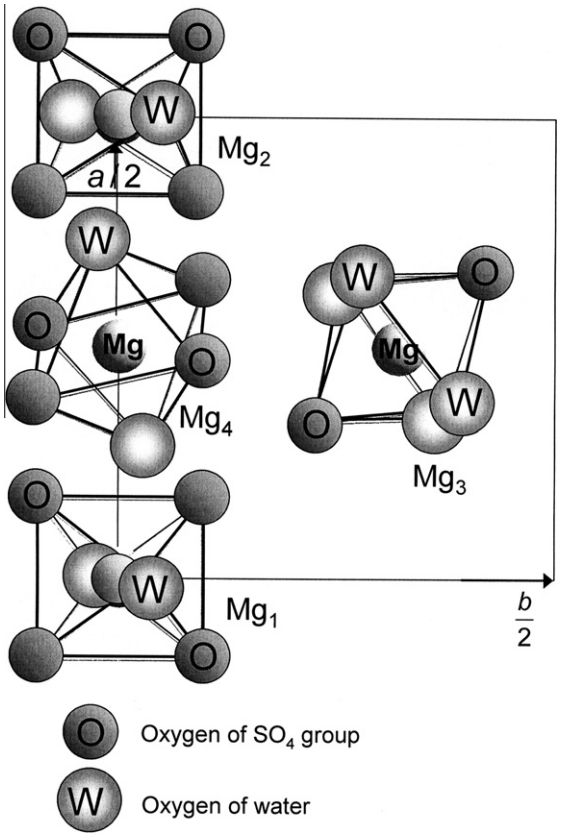

Fig. 3. Four structurally inequivalent magnesium octahedra Mg_1, Mg_2, Mg_3, and Mg_4 in the crystal unit cell. The Mg_3 site is substituted by doped Cu^{2+} ions.

evaporation leads to face rich crystals as it is shown in Fig. 4. Angular dependence of the EPR spectra has been collected in the orthogonal reference frames 1–3 related to the crystal habit and in crystallographic axes *a*, *b*, *c**. Measurements in the two frame increase accuracy of resulting spin-Hamiltonian parameters. Moreover, the principal directions of the *g* tensor lie very near the 12-plane, 23-plane and 31-plane allowing measurements of the temperature dependence and spin echo decay close to canonical orientations. Angular dependence of the spectra in *a*, *b*, *c** frame allows a direct relation between doped Cu^{2+} complex and the host crystal structure.

EPR measurements were performed in the temperature range 4.2–300 K with a Bruker ESP 380E FT/CW X-band spectrometer (pulse EPR experiments) and with a Radiopan SE/X 2547 spectrometer (cw-EPR experiments) equipped with Oxford flowing helium

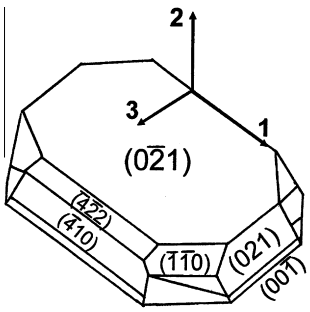

Fig. 4. Crystal habit of $KZnClSO_4{\cdot}3H_2O$ crystal with well developed (0$\bar{2}$1) plane. Experimental reference frame for EPR measurements is marked as 1–3 with the 1-axis along the longest edge and the two-axis perpendicular to the plane.

EPR cryostats. Both single crystal and powder spectra were recorded. Electron spin echo experiments were performed up to 60 K only since due to a shortening of the dephasing time at higher temperatures, the spin echo signal is lost in the dead time of the spectrometer. The experiments were performed along local *g*-factor *z*-axis (12-plane, $\Theta = 75°$) by excitation of the single hyperfine line $m_I = +1/2$. The hyperfine line and the lines from complexes A and B were well separated at this crystal orientation. Spin–lattice relaxation time T_1 was determined by spin echo saturation method with 16 ns saturation pulse and reading two-pulse echo sequence 16–176–16 ns. The full saturation was achieved in the whole temperature range. The electron spins echo dephasing described by the phase memory time T_M was determined by the Hahn-type echo amplitude after excitation by the above two-pulse sequence. The decay was strongly modulated allowing an analysis of the Fourier Transform spectra (electron spin echo envelope modulation = ESEEM).

4. Results and discussion

4.1. EPR spectra, angular dependence and spin-Hamiltonian parameters

EPR spectrum of Cu^{2+} in $KZnClSO_4{\cdot}3H_2O$ crystal consists of two quartets of equidistant hyperfine lines in most crystal orientations, except the rotation around the *b*-axis as expected for monoclinic crystal symmetry. The lines are relatively broad and overlap strongly at room temperature. For this reason a low accuracy parameters were determined in papers [9,10]. At very low temperatures a significant saturation effect deforms EPR spectra even for a very low microwave power. Thus, we performed measurements of angular dependence at liquid nitrogen temperature. EPR spectra recorded at 77 K along the principal *g* tensor directions for two equivalent complexes A and B are shown in Fig. 5. Except two marked hyperfine quartets, some additional lines are visible in between the B-complex lines in the upper trace. These lines arise from another Cu^{2+} complex different from complexes A and B. This indicates that except the occupation sites preferred by complexes A and B another site is also weakly occupied with spectral lines recognized in a few crystal orientations only. In the 12-plane at $\Theta = 75°$ (the lowest trace in Fig. 5) the forbidden transition line

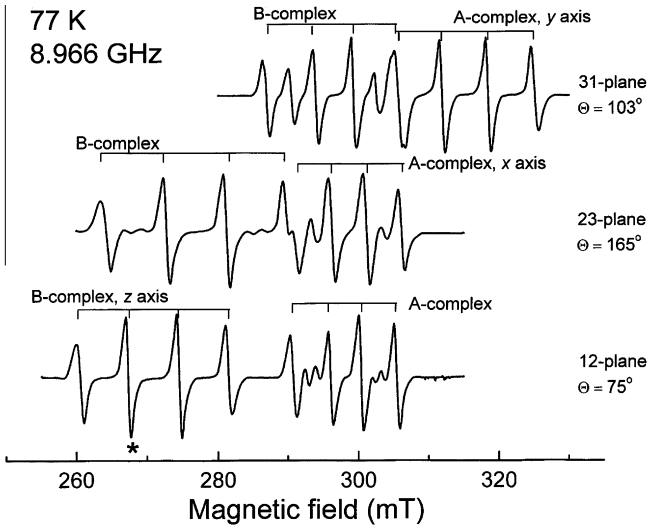

Fig. 5. EPR spectra recorded at 77 K along principal *g* tensor axes of two equivalent complexes A and B: *y*-axis for complex A (upper trace); *x*-axis of complex A (middle), and *z*-axis of the complex B (lower trace) accessible in the 1–3 reference frame. The asterisk mark line which has been excited during pulse EPR experiments.

doublets appear in between the high-field lines as usually observed in low symmetry complexes. The powder EPR spectrum is dominated by the lines from the dominant Cu^{2+} complexes without a trace of lines from the other complex or forbidden transitions (Fig. 6).

Angular dependence of the spectrum recorded in 1–3 laboratory frame plotted in Fig. 7 suggests that the principal direction of the g and A tensor coincide. Diagonalization of the experimental $\boldsymbol{g^2}$ and $\boldsymbol{gA^2g}$ tensors gives the spin-Hamiltonian parameters g and A (Table 2) and principal tensor axes direction cosines (Table 3) and confirms that the tensors have collinear principal axes. Solid lines in Fig. 7 are plots with these parameter values. The experimental results show that the A and B complexes have nearly perpendicular z-axes. Assuming that the z-axis is determined by water-water direction in complexes Zn_1, Zn_2, and Zn_4 and by SO_4–Zn–SO_4) direction in the complex Zn_3 we can recognize from Fig. 1 and Fig. 3 that mutually perpendicular z-axes exist for Zn_3 complexes only. Higher accuracy data concerning the Cu^{2+} localization in the crystal unit cell were derived from angular variations measurements in a, b, c^* reference frame. They give the same principal g and A tensor values as above and principal axes direction cosines listed in Table 3 (errors in parameters indicated in Table 2 are determined from differences between measurements in both reference frames). It should be noted that the g and A value are consistent with these determined from powder spectrum at points marked in Fig. 6, where experimental and simulated powder spectra are compared.

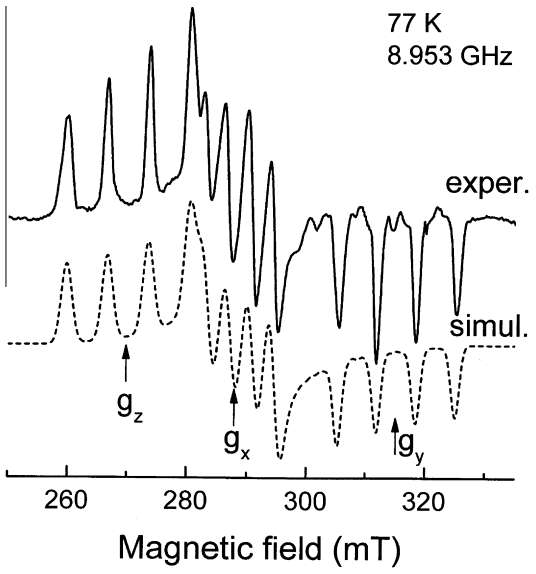

Fig. 6. Powder EPR spectrum recorded at 77 K computer simulated spectrum (dashed line) using SimFonia routine with the g-factors and hyperfine splitting given in Table 2 and corresponding peak-to-peak Gaussian line: 1.8 mT (z-axis), 1.4 mT (y-axis), and 1.8 mT (x-axis).

A comparison of the x, y, and z direction cosines with these for the trans–ligand directions in Zn_3 octahedron is given in Table 3. Although Cu^{2+} deforms the host Zn_3 environment (as shown by strong g-factor anisotropy) the local crystal field axes are close to those in the unperturbed structure. The z-axis (octahedron elongation axis) deviation from the apical O_7^{145}—O_7^{142} direction is 4.6° only. The x and y axes are slightly rotated with respect to the trans ligand –ligand directions (8.2° for y-axis, and 5.8° for x-axis) as it is expected when d-orbital mixing is allowed by low crystal field symmetry [12]. The localization of the doped Cu^{2+} ions at Zn_3 site is confirmed by pulsed EPR measurements as it is discussed in a next section.

The g and A-values are not significantly different from those published for $KMgClSO_4{\cdot}3H_2O$ and $KZnClSO_4{\cdot}3H_2O$ crystals (Table 2). However, the A and B complexes were previously described as non-equivalent and the principal x, y, and z-axes were differently assigned. In fact, the interpretation of the results is not trivial since the g- and A-values are not typical of most of the Cu^{2+} complexes. At first sight it is difficult to assign z, y, and x axes from relative value of the three experimental g-factors or from the A-values showing unusually low anisotropy. It has to be related to a low symmetry of the crystal field at Cu^{2+} site. The lowest g-factor value is lower than 2.04. This can be due to a mixing of d-orbitals in the ground state at the low symmetry. However, independently of the ground state, the maximal hyperfine splitting always appears along the z-axis since it is mainly determined by electron–nucleus dipolar coupling, which always dominates the g-factor anisotropy contributions. Thus g_z can be assigned as the maximal g-factor value indicating that the $d_{x^2-y^2}$ orbital dominates in the ground state. An unusual sequence and values of the spin-Hamiltonian parameters are explained by analysis in terms of molecular orbital (MO) theory.

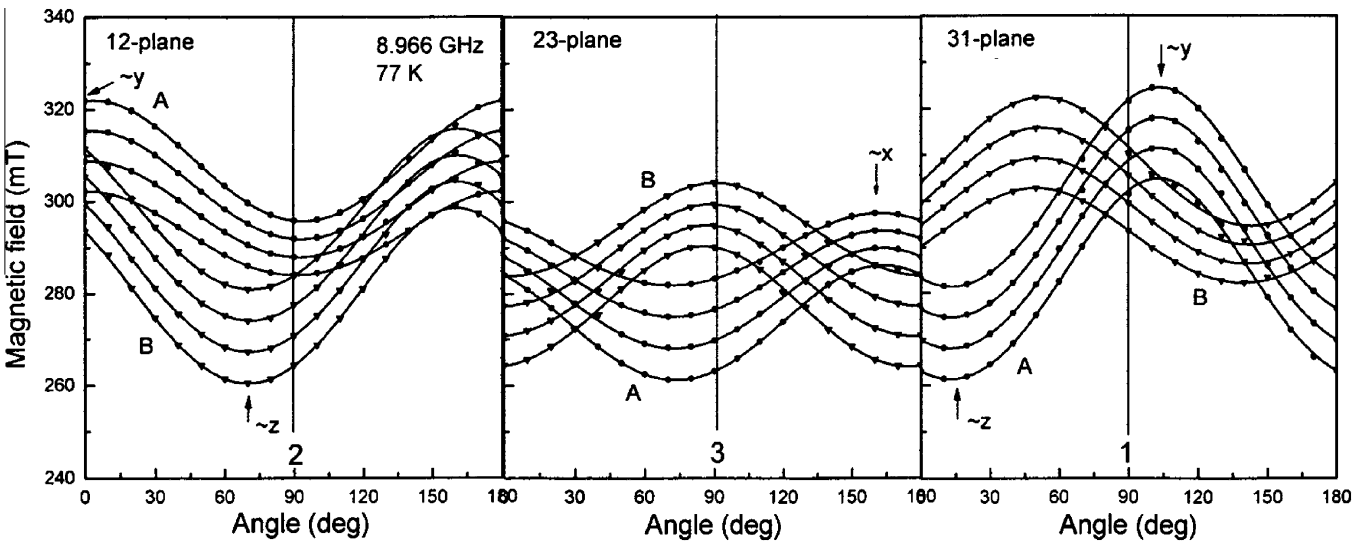

Fig. 7. Angular variations of the line positions in three planes of the 1–3 reference frame at 77 K. Lines from complexes A and B are marked. Arrows indicate positions close to the local principal axes x, y, z of the complexes.

Table 2
EPR spin–Hamiltonian parameters (A-values in 10^{-4} cm^{-1}). The signs of A-values were determined from MO-theory analysis.

g_z	g_y	g_x	A_z	A_y	A_x	T (K)	Ref.
2.3717(5)	2.0335(7)	2.1996(7)	−76.4(8)	62.7(7)	−38.0(7)	77	This paper
2.4247	2.0331	2.1535	−103	63	−31	4.2	
2.294	2.039	2.229	59	48	50	295	[10]
2.351	2.034	2.204	67	43	54	123	[6]

Table 3
Direction cosines of g tensor and A tensor principal axes and the O–O directions in Cu^{2+} complex at Zn_3 site.

	In laboratory frame 1–3					
	Complex A			Complex B		
	z axis	y axis	x axis	z axis	y axis	x axis
1	0.2016	0.9659	0.1626	0.3651	0.8067	−0.4647
2	0.2594	0.1074	−0.9598	0.9161	−0.2223	0.3338
3	0.944	−0.2356	0.2289	−0.1659	0.5475	0.8202
	In crystallographic axes a, b, c^*			Trans- oxygen ligand directions		
	z axis	y axis	x axis	Apical O_7^{145}—O_7^{142}	Equatorial W_6^{194}—W_7^{197}	Equatorial W_3^{173}—W_3^{170}
a	∓0.7012	∓0.5151	±0.4931	∓0.7558	∓0.4554	±0.4058
b	−0.7046	0.3935	−0.5906	−0.6437	0.5171	−0.6021
c^*	±0.1102	∓0.7614	∓0.6388	±0.1203	∓0.7247	∓0.6876

4.2. Electronic structure of Cu^{2+} complexes (MO-theory analysis)

The g and A tensor values suggest the D_{2h} crystal field symmetry. In D_{2h} symmetry the d-orbitals are mixed with s-orbital as allowed by the point symmetry and anti-bonding molecular orbitals of the Cu^{2+} complex are

$$\begin{aligned}
&\Psi(A_g) = \alpha(ad_{x^2-y^2} + bd_{z^2} + c_s s) - \alpha' L_1\\
&\Psi(A_g') = \alpha_1(ad_{z^2} - bd_{x^2-y^2} + c_s' s) - \alpha_1' L_2\\
&\Psi(B_{1g}) = \beta_1 d_{xy} - \beta_1' L_3\\
&\Psi(B_{2g}) = \beta d_{xz} - \beta' L_4\\
&\Psi(B_{3g}) = \beta' d_{yz} - \beta'' L_5\\
&a^2 + b^2 + c_s^2 = 1
\end{aligned} \tag{1}$$

For the A_g ground state symmetry the principal g tensor and A tensor components are [13]:

$$\begin{aligned}
g_z &= 2.0023 - 8\alpha^2\beta_1^2 a^2 \frac{\lambda}{E_{xy}}\\
g_y &= 2.0023 - 2\alpha^2\beta^2\left(a - \sqrt{3}b\right)^2 \frac{\lambda}{E_{xz}}\\
g_x &= 2.0023 - 2\alpha^2\beta^2\left(a + \sqrt{3}b\right)^2 \frac{\lambda}{E_{yz}}
\end{aligned} \tag{2}$$

$$\begin{aligned}
A_z &= \alpha^2 c_s^2 A_{4s} + P\left[-\alpha^2\kappa + \Delta g_z - \frac{4}{7}\alpha^2(a^2 - b^2)\right.\\
&\qquad \left. + \frac{1}{14}\frac{3a + \sqrt{3}b}{a - \sqrt{3}b}\Delta g_y + \frac{1}{14}\frac{3a - \sqrt{3}b}{a + \sqrt{3}b}\Delta g_x\right]\\
A_y &= \alpha^2 c_s^2 A_{4s} + P\left[-\alpha^2\kappa + \Delta g_y + \frac{2}{7}\alpha^2\left(a^2 - b^2 + 2\sqrt{3}ab\right)\right.\\
&\qquad \left. - \frac{\sqrt{3}}{14}\frac{b}{a}\Delta g_z - \frac{1}{14}\frac{3a - \sqrt{3}b}{a + \sqrt{3}b}\Delta g_x\right]\\
A_x &= \alpha^2 c_s^2 A_{4s} + P\left[-\alpha^2\kappa + \Delta g_x + \frac{2}{7}\alpha^2\left(a^2 - b^2 - 2\sqrt{3}ab\right)\right.\\
&\qquad \left. + \frac{\sqrt{3}}{14}\frac{b}{a}\Delta g_z - \frac{1}{14}\frac{3a + \sqrt{3}b}{a - \sqrt{3}b}\Delta g_y\right]
\end{aligned} \tag{3}$$

where $\lambda = -829$ cm^{-1} is the spin–orbit coupling, $P = 0.036$ cm^{-1} represents average extension of the d-orbital and κ is the Fermi contact interaction parameter which is equal to 0.43 for free Cu^{2+} ion. E_{ij} are orbital energies and $\Delta g_i = g_i - 2.0023$. The exact orbital energy values are unknown and are treated as a fitting parameters, since the optical absorption spectrum is a broad asymmetrical band centered at around 11,900 cm^{-1} [6]. The first term in expressions for A_i is an isotropic contribution of the 4s-orbital to the hyperfine splitting. This term is small and usually is omitted in the analysis of data.

Because the EPR parameter depend on temperature, the discussion in terms of MO-theory should be performed for rigid lattice results only, i.e., for data collected below 20 K in our crystal. An evaluation of the ground state parameters from data collected at 77 K, as it has been done in previous papers, is invalid because the g-factors and hyperfine splitting are dynamically averaged at this temperature. Thus, our analysis is performed for data collected at 4.2 K with parameters shown in Table 2. Using these data we can calculate three parameters from Eq. (3), i.e., a, α^2, and κ. Their values depend on the signs of A_i. The A_z-value is negative as is directly visible in Eq. (3), and only $A_y > 0$, and $A_x < 0$ gives acceptable parameter values of Eq. (3). These are listed in Table 4. Eq. (2) and experimental g-values at rigid lattice limit allow to calculate orbital energies E_{ij} *vs.* covalency parameters β_i. For all β_i-parameter values, with maximal value equal to 1, the sequence of the orbital energies is as usually expected in elongated octahedral coordination with $E_{yz} > E_{xz} > E_{xy}$, but a choice of the β_i-values is dictated by UV–Vis spectrum. The spectrum is already published [6], and its decomposition on Gaussian components (a broad background line is omitted) consistent with our calculations is shown in Fig. 8. The evaluated energies and parameters are collected in Table 4. The covalency parameters β_i describe the degree of delocalization of the unpaired electron spin density *via* the excited orbital states. Delocalization from the ground state $d_{x^2-y^2}$ (7%) is rather small compared to a much larger delocalization *via* in-plane d_{xy} orbital (20%). Considerable delocalization appears *via* out-of-plane orbitals d_{yz} and d_{xz}. It results from an overlap between the lobs of these orbitals and 3p-orbitals of chlorine atoms asymmetrically located in the vicinity of apical oxygen ligand positions.

Table 4
Calculated energy of *d*–*d* transitions and MO parameters.

E_{xy} = 11,000 cm^{-1}		E_{xz} = 11,700 cm^{-1}		E_{yz} = 13,100 cm^{-1}	
α^2 = 0.947	α'^2 = 0.93	β_1^2 = 0.80	β^2 = 0.71	$\beta^{2\prime}$ = 0.67	κ = 0.284

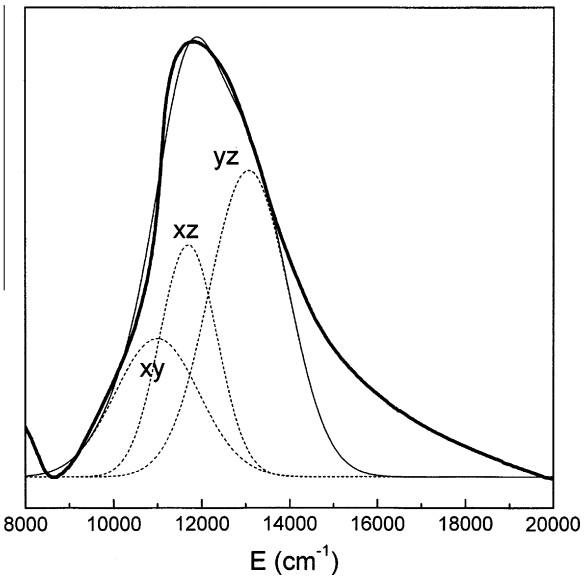

Fig. 8. UV–Vis spectrum [6] and three Gaussian components located at positions determined from the EPR *g*-values.

The ground state of Cu^{2+} contains small admixture of the d_{z^2} orbital and can be written as $|0\rangle = 0.96(0.97|x^2 - y^2\rangle + 0.03|z^2\rangle)$. Despite the small d_{z^2} admixture the mixing has a significant effect on the *g*-factor values: g_z decreases, g_x increases and becomes much larger than g_y which tends to $g_y = 2$ [14]. This behavior is shown for our case in Fig. 9, with the inset demonstrating the crossing point between g_x and g_y.

Untypical EPR of Cu^{2+} complexes in $KZnClSO_4{\cdot}3H_2O$ crystal, i.e., the sequence $g_z > g_x > g_y$, the small anisotropy of hyperfine interaction are due to mixing of orbitals in the ground state at low crystal field symmetry at the Cu^{2+} sites. The low crystal field symmetry results from deformation of the coordination octahedron by asymmetric hydrogen bonds to sulfate groups, and by asymmetric positions of the nearest chlorine atoms interacting with excited orbital states of Cu^{2+} ion.

4.3. Temperature dependence of the spin-Hamiltonian parameters

EPR spectrum varies with temperature. Single crystal and powder spectra show continuous shift in *g*-values and hyperfine splitting *A* on heating, towards its average values. This appears along local *x* and *z* directions only, whereas g_y and A_y are unchanged (Fig. 10). Traces of the $\boldsymbol{g^2}$ and $\boldsymbol{gA^2g}$ tensors keep constant and directions of the *x*, *y*, and *z*-axis are not affected. This is typical motional averaging (merging effect) resulting from jumps between two configurations (two potential wells) of the Cu^{2+} complex having different energies. The well resolved lines at low temperatures first broaden and shift on heating, then coalesce into a single line when jumping frequency sufficiently increases as compared to the line splitting. The potential wells are produced by the Jahn–Teller effect which is responsible for a strong axial distortion of the Cu^{2+} coordination octahedron as it is indicated by strong *g*-factor rhombicity. At low temperatures, below of about 20 K, all Cu^{2+} complexes are localized in the deepest potential well and the low temperature EPR spectrum does not show any trace of the spectrum from the two other wells. The increase in temperature leads to transitions between the two lowest energy wells, without localization in the higher energy well. This effect can be described in frames of the classical motional averaging theory or vibronic averaging model. Both approaches have some drawbacks and are outlined below.

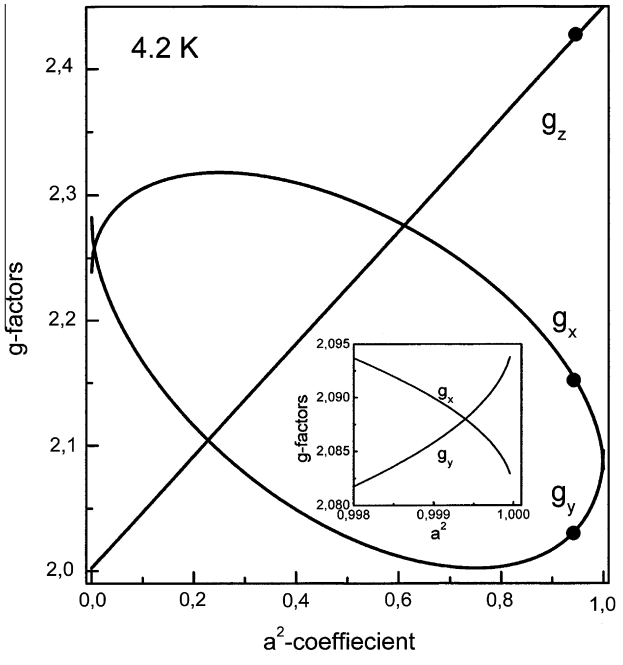

Fig. 9. Dependence of *g*-factors on the orbital mixing coefficient a^2 in the ground state calculated from Eq. (2) with parameters of Table 4. Full circles indicate experimental g-values of our Cu^{2+} complex at 4.2 K, i.e., for rigid lattice.

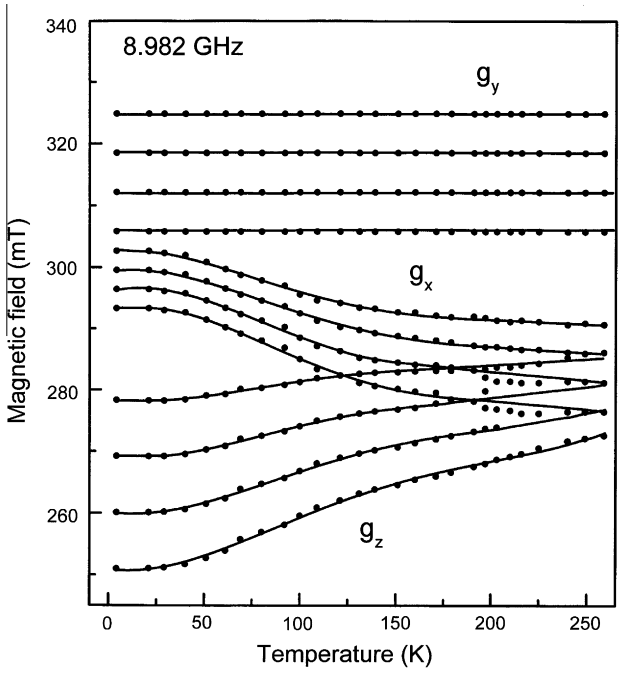

Fig. 10. Temperature variation of the line positions. Solid lines are guides for the eyes only.

Classical motional averaging theory can be formulated in terms of general Kubo–Tomita theory [15], which leads to a complicated description by correlation functions and it does not allow a straightforward description of experimental results [16]. Another, commonly used approach is an adapting of the Bloch equation to include the jumps or exchange of sub-system magnetizations [17]. The above theories are used in description of motional averaging effects in hyperfine structure of free radicals with isotropic g-factor. We have generalized this description for the case of different g-factors [18,19]. This is essential in description of exchange averaging effects for Cu^{2+} displaying strong g-factor anisotropy.

EPR spectrum (the first derivative of absorption) of two Lorentzian lines A and B having different g-factors, affected by jumps of frequency f has the shape $Y(B)$:

$$Y(B) = N\frac{[W_2 - 2(B-B_0)f](W_1^2+W_2^2) - 4[(B-B_0)W_2 - (\Gamma_0+2f)W_1][(B-B_0)W_1 - (\Gamma_0+f)W_2]}{(W_1^2+W_2^2)^2}$$

$$\begin{aligned} W_1 &= (B-B_A)(B-B_B) - \left[\Gamma_A + 2f\frac{g_B}{g_A+g_B}\right]\left[\Gamma_B + 2f\frac{g_A}{g_A+g_B}\right] \\ &\quad + 4f^2\frac{g_A g_B}{(g_A+g_B)^2} \\ W_2 &= (B-B_A)\left[\Gamma_B + 2f\frac{g_A}{g_A+g_B}\right] + (B-B_B)\left[\Gamma_A + 2f\frac{g_B}{g_A+g_B}\right] \end{aligned} \quad (4)$$

Resonance fields of the lines at rigid limit are $B_A = 71.4484\nu_0/g_A$ and $B_B = 71.4484\nu_0/g_B$.

The half-field linewidth Γ is related to the peak-to peak linewidth $\Gamma_{A,B} = \left(\sqrt{3}/2\right)\Delta B_{pp}^{(A,B)}$.

$\Gamma_0 = (\Gamma_A + \Gamma_B)/2$, $B_0 = (B_A + B_B)/2$. All parameters are given in mT and $f(\mathrm{mT}) = 0.0357[(g_A+g_B)/(g_A g_B)]f(\mathrm{MHz})$. N is a normalization factor.

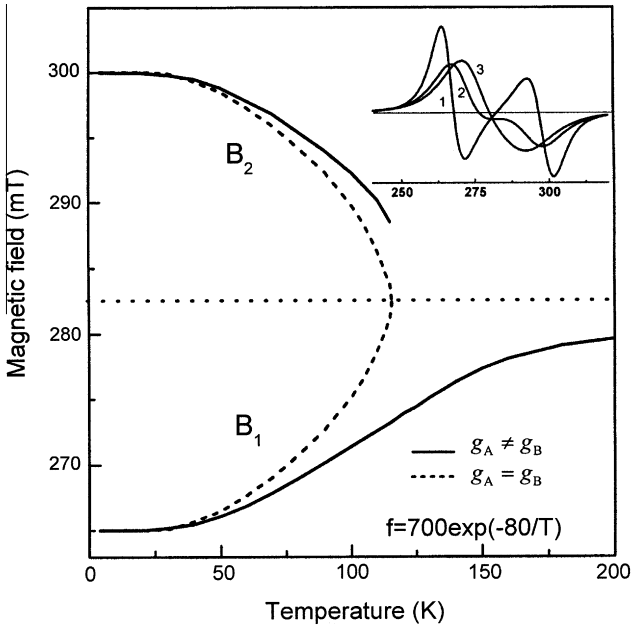

Fig. 11. Motional averaging of the two-line positions $B_A = 265$ mT and $B_B = 300$ mT due to jumps with temperature dependent frequency $f = 700\exp(-80/T)$ for lines having different g-factors (solid lines) or having identical g-factors (dashed lines). B_1 and B_2 are fields where absorption spectrum has maxima (where derivative spectrum amplitude is equal to zero) as it can be recognized for averaged lines of initial width 0.1 mT at: (1) 70 K, (2) 140 K, and (3) 220 K (see the inset). The two-line spectra in the inset were generated using Eq. (4).

The difference in the g-factors significantly influences temperature averaging compared to that expected when $g_A = g_B$. It is shown in Fig. 11 where both cases are compared. The collapse of lines having identical g-factors is symmetrical and appears at a lower temperature. The difference in g-factors produces asymmetric line coalescence. Moreover, the high-field line position can be determined directly from the spectrum for low temperatures only. For highest temperatures the derivative has no zero-value. It can be recognized from the inset of Fig. 11 where the shape of two-component spectrum is shown at different temperatures as calculated from Eq. (4). A general observation is that even for two identical and very narrow lines having different g-factors the averaging is asymmetric (high-field line is more broadened) and is expanded for a larger temperature range.

Our goal is the determination of the jump frequency f from experimentally measured line positions B (g-factors). These can be found as peaks in absorption spectrum at points where first derivative is equal to zero, i.e., $Y(B) = 0$. The linewidth can be taken as $\Gamma = 0$ because not the lineshape but g-factors will be analyzed. Thus, the jump frequency can be calculated from Eq. (4) as:

$$f^2 = \frac{4KW_1(B-B_0)^2 - KW_1^2 - 3(B-B_0)W_1^2}{4K^3 + 8KW_1 - 12K^2(B-B_0)} \quad (5)$$

where

$$K = (B-B_A)\frac{g_A}{g_A+g_B} + (B-B_B)\frac{g_B}{g_A+g_B},$$

B is position of the shifted line, i.e., B_1 or B_2 for line A and B, respectively. Eq. (4) reduces to well known expression $B_2 - B_1 = \sqrt{(B_A-B_B)^2 - 8f^2}$ for $g_A = g_B$. Eq. (5) can be used for fre-

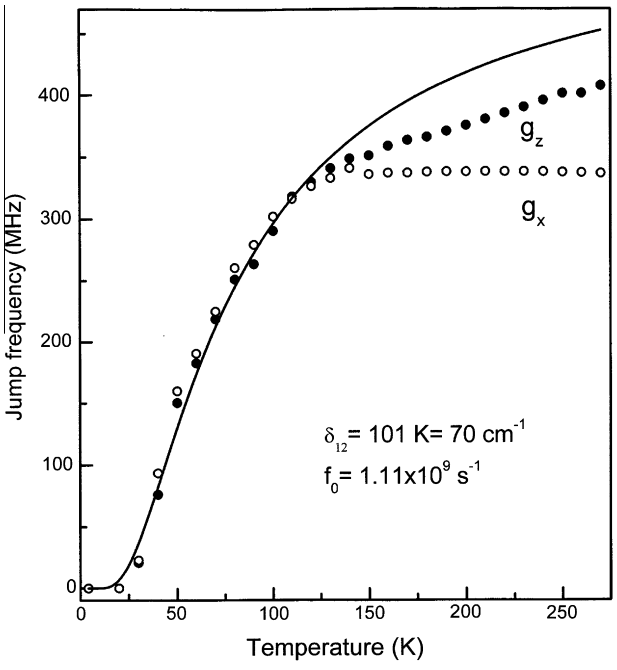

Fig. 12. Jump frequency temperature dependence calculated using Eq. (5) from two resonance fields corresponding to g_x (open circles) and g_z (full circles). The solid line is the fit to Eq. (6).

quency f determination separately from $B = B_1$ or $B = B_2$. Taking $B_1 = 71.4484\nu_0/g_z$ and $B_2 = 71.4484\nu_0/g_x$ from data presented in Fig. 10 we have calculated temperature dependent f-values as sit is presented in Fig. 12. An assumption of the over-barrier jumps described by Arrhenius equation $f = f_0 \exp(-\delta_{12}/kT)$ leads to parameters $f_0 = 0.5 \times 10^9\ s^{-1}$ and unrealistically low energy barrier $\delta_{12} = 60\ K = 42\ cm^{-1}$. Thus, classical over-barrier jumps can be excluded. Other mechanisms of the barrier crossing between non-equivalent potential wells should be considered as phonon induced tunneling (tunneling through oscillating barrier) or phonon controlled tunneling *via* excited vibrational (or vibronic) level. The first mechanism producing incoherent tunneling is driven by phonon motions and leads to temperature dependent jump frequency proportional do T (for direct phonon process) and proportional to T^3 or T^7 for Raman phonon process [20,21]. These dependencies do not fit our experimental data. The second mechanism including energy difference ΔU between the wells gives temperature dependence of tunneling frequency in excited state of energy δ_{12} in the form [22]:

$$f = f_0 \frac{1}{1 + \exp(-\delta_{12}/kT)} \tag{6}$$

where the pre-exponential factor is not simply an attempt frequency, as usually, but depends on the probability of tunneling, the width of the excited vibrational level and energy difference ΔU between the wells.

Solid line in Fig. 12 is the best fit to Eq. (6) with $f_0 = 1.1 \times 10^9\ s^{-1}$ and $\delta_{12} = 101\ K = 70\ cm^{-1}$. Thus, the mechanism of coherent tunneling in excited state involves thermal excitation of energy $70\ cm^{-1}$, tunneling through the barrier and decay to the ground state in the second well. This mechanism, if effective, warrants Boltzmann population of both wells when only deepest well is occupied at very low temperatures as it is in our case.

It is visible from Fig. 12, that apparent line positions (g-factors) experimentally determined for temperatures larger than 120 K are disturbed by line broadening and are not useful when Eq. (4) is applied.

The question is if we would obtain the same value of f_0 and δ_{12} if another averaging model is applied. The widely used is phenomenological Silver–Getz model [23] modified by Riley–Hitchman [24], which assumes that the observed g-factors are the weighted averages of the potential well population. Since the highest energy well is not populated in the studied temperature range (as shown by temperature independent g_y-factor) the experimental g-factors can be calculated as

$$\begin{aligned} g_z(T) &= N_1 g^0_{z1} + N_2 g^0_{x2} \\ g_x(T) &= N_1 g^0_{x1} + N_2 g^0_{z2} \end{aligned} \tag{7}$$

where N_i is the well population with $N_1 + N_2 = 1$ and g^0_{ik} is the rigid limit g-factors ($i = x, z$) in first and the second well ($k = 1, 2$). The Silver–Getz model assumes that the g-factors are identical in both wells and then the well's populations can be calculated from experimental g-factor values as $N_2 = (g_z(T) - g^0_z)/(g^0_x - g^0_z) = (g_x(T) - g^0_x)/(g^0_z - g^0_x)$. Assuming the Boltzmann well population the energy difference between the wells can be evaluated as $\delta_{12} = -kT \ln(N_1/N_2)$.

Temperature variations of g_z and g_x are shown in Fig. 13 where calculated barrier height is also presented. The Silver–Getz model assumes that the barrier δ_{12} is temperature independent. In our case it is true for temperatures larger than about 120 K with $\delta_{12} = 118\ K = 82\ cm^{-1}$. This value is close to that determined from results of previous model shown in Fig. 12. Application of the Silver–Getz model to Cu^{2+} complexes in Tutton salts [25,26] and in $Cd(HCOO)_2{\cdot}2H_2O$ [27] confirms that the δ_{12} varies with temperature suggesting restricted validity of the model.

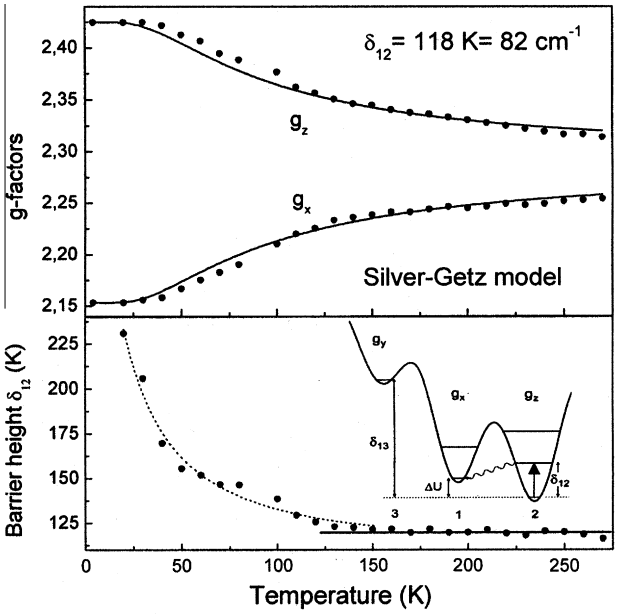

Fig. 13. The g-factor temperature dependence (upper) with fit to the Silver–Getz model (solid line) with jumping between two potential wells differ in energy of $\delta_{12} = 82\ cm^{-1}$, as estimated from the straight line in the barrier height temperature dependence (lower). The inset shows the two-well model parameters used in discussion of the results. The $g_y = 2.0335$ and is temperature independent.

A decrease δ_{12} on heating below 120 K indicates that the Silver–Getz model assumption of Boltzmann population is not fulfilled at low temperatures. We have drawn the similar conclusion from Cu^{2+} behavior in $(NH_4)_2Mg(SO_4)_2{\cdot}6H_2O$ [28]. This suggests that the phonon induced tunneling *via* excited vibrational state of energy δ_{12} being intra-well jumps mechanism, as we discussed above, is not sufficiently effective at low temperatures. This conclusion is clearly supported by the observation that the model with Boltzmann population starts to be valid at a temperature where thermal energy is comparable with excited vibrational level energy, i.e., of about 120 K. Boltzmann population exists between vibrational levels in every well but not necessary between the wells at low temperatures. The deviation from the Boltzmann population is also visible in theoretical plots (solid lines in the upper plots of Fig. 13).

Simultaneously with the g-factors the hyperfine splitting is dynamically averaged as it is presented ion Fig. 14. However, it tends to an averaged value lower than the expected $(A^0_z + A^0_x)/2$ value. We have observed a similar behavior for Cu^{2+}in other crystals with the dynamical Jahn–Teller effect [27–30]. From Eq. (3) it is visible that it can be explained as due to a decrease in value of the MO-coefficient α^2 or value of the Fermi constant κ. Assuming that $\kappa = 0.284$ is temperature independent, as intra-ionic parameter, we calculated the temperature variation of α^2 from Eq. (3). This is shown in the lower part of Fig. 14. Nearly linear decrease of α^2 on heating displays continuous increase of the delocalization of the unpaired electron spin density on the ligands in the water-coordination plane. Correction of the measured $A(T)$ dependence taking into account the $\alpha^2(T)$ effect leads to the temperature dependence shown by open circles in Fig. 14. Theoretical plots of Silver–Getz model are shown by the solid lines. This figure confirms that there is a clear deviation of the model assuming the Boltzmann population from the experimental point at low temperatures.

Both motional averaging models presented above give similar barrier height for the inter-well jumps and can be consistently interpreted in terms of phonon induced tunneling in excited vibrational state. The models have some simplification assumptions.

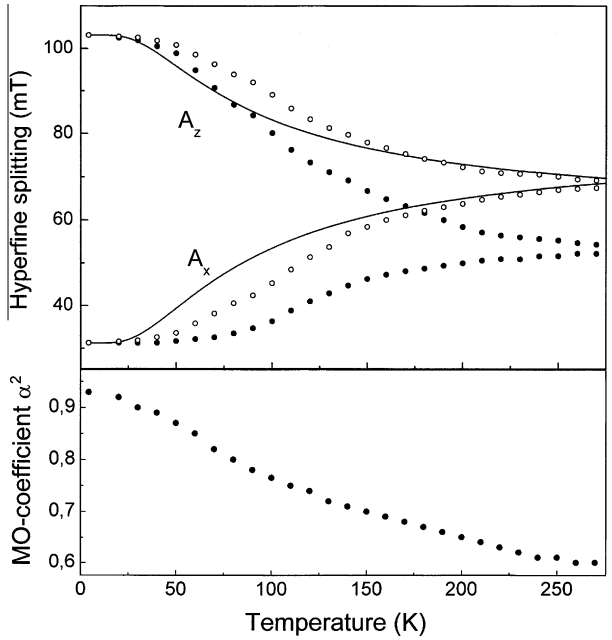

Fig. 14. Temperature dependence of the hyperfine splitting A (upper) and electron spin density coefficient α^2 in the ground state (lower). Experimental points are marked with full circles. Open circles show results corrected for α^2 temperature dependence with solid line being fit with Eq. (3). The $A_y = 62.7 \times 10^{-4}\,cm^{-1}$ is temperature independent.

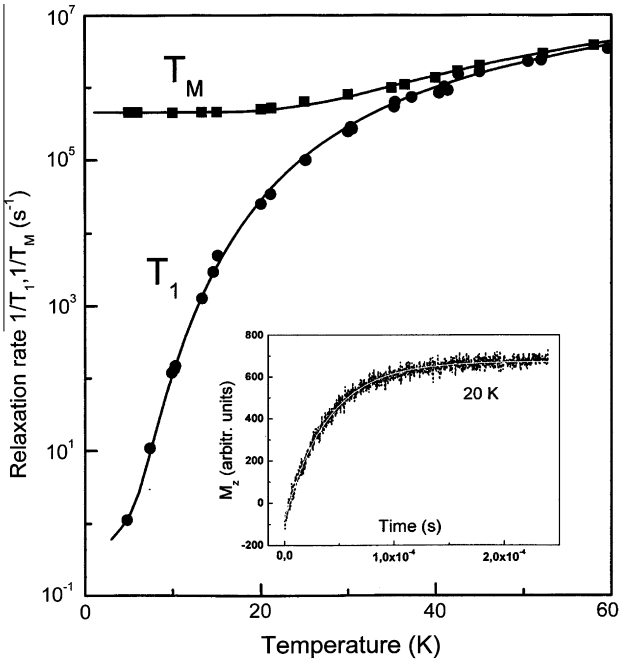

Fig. 15. Temperature dependence of the spin–lattice $1/T_1$ (points) and phase memory $1/T_M$ (squares) rates. Solid lines are fits to Eqs. (9) and (10), respectively. The inset presents magnetization recovery at 20 K with single exponential fit with $T_1 = 39$ μs (solid line).

The Silver–Getz model assumes the Boltzmann population of the wells produced by Jahn–Teller always exists, whereas the model based on the generalized Bloch equations does not take the Boltzmann population into account at all. Silver–Getz model gives barrier energy only, whereas the second model gives also the jump frequency. The first model is valid at higher temperatures where thermal energy is higher than δ_{12}, whereas the second model is valid at lower temperatures even when the Boltzmann population of the wells is not achieved yet.

Our results suggest that a direct tunneling does not operate between the ground vibrational states in the two neighboring wells. It means that the tunneling splitting of the ground state is much smaller than the energy difference ΔU between the wells and moreover, an incoherent phonon-assisted tunneling *via* oscillating barrier is not effective.

4.4. Electron spin relaxation and ESEEM spectroscopy

In the course of pulsed EPR experiments we have measured spin–lattice relaxation time T_1 and electron spin echo decay described by the phase memory time T_M. At first step we determined T_1 and T_M along local g tensor direction x, y, and z. No considerable difference was found. Thus, temperature dependence was recorded along the z-axis only by pulsed excitation of the line marked by asterisk in Fig. 5 in the temperature range 4.2–60 K. Above 60 K the electron spin echo signal decay becomes very fast because EPR lines become homogeneously broadened. As a result the echo signal decays in the dead time of the spectrometer (about 80 ns). The spin–lattice relaxation time was determined from the recovery of magnetization formed after pulse excitation. The magnetization decay was monitored by two-pulse ESE signal amplitude decay. The recovery was exponential in the whole temperature range and described by the following equation:

$$M = M_0\left[1 - \left(\frac{M_1}{M_0}\right)\exp\left(-\frac{t}{T_1}\right)\right] \tag{8}$$

where M_0 is the equilibrium magnetization (for $t \to \infty$) and M_1 is the initial magnetization value after excitation (for $t = 0$). The recovery of magnetization at 20 K is shown in the inset of Fig. 15, where the solid line is the fit to Eq. (8). The relaxation rate $1/T_1$ is temperature dependent as it is shown in Fig. 15. Strong acceleration of the relaxation rate with temperature is characteristic for two-phonon Raman relaxation processes [31] which, in Debye's model of phonon vibrations, can be described as [32]:

$$\frac{1}{T_1}(Raman) = \frac{9\hbar^3}{k_B}\left(6\pi^{11/10}\frac{pN_A}{M}\rho^{2/5}\right)^{10/3}\left(\frac{\langle s_1|V^{(1)}|s_2\rangle}{\Delta_{cr}}\right)^4 \times \frac{T^9}{\Theta_D^{10}}I_8(\Theta_D/T) = c'\frac{T^9}{\Theta_D^{10}}I_8(\Theta_D/T) \tag{9}$$

where p is the number of atoms in vibrating molecule, N_A the Avogadro's number, M the molecular weight of a compound, ρ the crystal density, and Δ_c is the orbital splitting corresponding to appropriate g-factor (in our case g_z). These parameters describe properties of the studied material and can be known *a priori*. The spin-phonon coupling parameter $\langle s_1|V^{(1)}|s_2\rangle$ is unknown and cannot be theoretically calculated (only roughly estimated). Thus, usually the above equation is parameterized to the lower form of Eq. (9) where the only fitting parameter is the Debye temperature Θ_D when it is not available. An analytical form of the transport integral I_8 is already known [33]. When Θ_D is known the spin-phonon coupling can be determined from experimental data and Eq. (9). Thus, although the $1/T_1$ (T) dependence is a smooth and monotonic curve one can obtain explicitly one of the parameters. Our results are well fit with parameters $c' = 2.8 \times 10^{-12}\,K^{-9}\,s^{-1}$ and $\Theta_D = 172$ K, but small term bT linear with temperature had to be added with $b = 0.2\,K^{-1}\,s^{-1}$. The plot with these parameters is shown by solid line in Fig. 15. The spin relaxation Debye temperature value is usually lower than that determined from specific heat or elastic constants measurements [32], thus it should be treated as lower limit of possible Θ_D. Lowering of Θ_D from its calorimetric value is due to a contribution of a local mode of vibration usually appearing for doped Cu^{2+} ions [32].

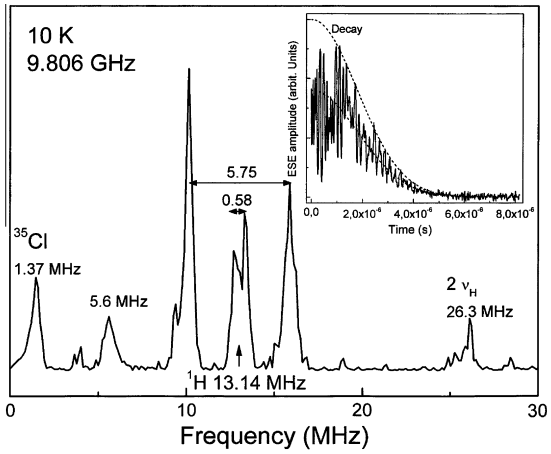

Fig. 16. ESEEM spectrum obtained as Fourier Transform of the echo modulations recorded at 10 K and 9.806 GHz. The decaying echo amplitude is presented in the inset with two decay functions (dashed lines): upper for T_M determination; lower for subtraction before the Fourier transformation.

Electron spin echo amplitude V decreases when interpulse interval τ increases. This is due to a dephasing of the precession motion of spins after excitation. The echo amplitude is strongly modulated as it is shown in the inset of Fig. 16. Thus, the effective decay function can be written as $V = V_{decay} \cdot V_{mod}$. The decay function V_{decay} is an envelope of the modulated decay as shown by a dashed line (upper) in the inset and can be described as $V_{decay} = V_0 \exp(-b\tau - m\tau^2)$ [34,35]. The first term describes temperature independent contribution from instantaneous diffusion and from temperature dependent spin–lattice relaxation processes with b-coefficient increasing with temperature. The second term describes temperature independent contribution from spectral diffusion. The temperature independent contributions dominate at low temperatures below 15 K. An effective phase memory time T_M was determined as the time where the decay function falls down to the V/e of its initial value. Dephasing rate $1/T_M$ slowly increases with temperature as it is presented in Fig. 15 and described as

$$\frac{1}{T_M(T)} = \frac{1}{T_M^0} + \frac{1}{T_1(T)} \tag{10}$$

where temperature independent contribution is $1/T_M^0 = 0.45 \times 10^6\ s^{-1}$ and the term $1/T_1$ is given by Eq. (9). The $1/T_M^0$-value is typical for a dephasing produced by the instantaneous diffusion between excited spins forming echo signal [34,36] whereas the temperature dependent contribution arises solely from the spin–lattice relaxation.

The electron spin echo amplitude modulations V_{mod} are due to weak dipolar coupling with surrounding magnetic nuclei. After subtraction of the decay function (lower dashed line in Fig. 16) the modulation function suitable for Fourier transformation was obtained. The Fourier Transform gives pseudo-ENDOR spectrum (ESEEM spectrum) with peaks at Larmor frequency of modulating nuclei and its harmonics. The spectrum is shown in Fig. 16. The spectrum is dominated by peaks produced by ^1H nuclei around proton Larmor frequency 13.14 MHz and contains a peak from chlorine nuclei at 1.37 MHz. The peak at of about 5.6 MHz cannot be directly assigned. It can be due to harmonic or sub-harmonic of basic frequencies or their combinations like a combination of the main peak frequencies at 10 MHz and 16 MHz, or a four-harmonic of chlorine frequency. The proton peaks consist of the intensive doublet with splitting of 5.75 MHz, weak doublet with splitting of 0.58 MHz overlapping the matrix line from distant nuclei, and the first harmonic line at about 26.3 MHz. The strong doublet arises from protons located at distance 0.245 nm from Cu^{2+} (in point dipole approximation). The high intensity of the doublet line indicates a considerable amount of equivalent modulating protons. They can be identified as belonging to the coordinating water molecules. Such a situation appears when magnetic field is aligned along the z-axis of Cu^{2+} complex at Zn_3 site (as in our electron spin echo experiments), where eight protons in nearly equivalent positions exist. It does not appear, however, for the other Zn-sites. Thus, electron spin echo measurements confirm that doped Cu^{2+} ions are located at Zn_3 sites. The weakly split doublet superimposed on the matrix proton line arises from water molecule protons located at distance of about 0.55 nm. They can belong to the two water molecules marked as W_5 (one of them marked as W_5^{186} is visible in Fig. 2) at distance 0.521 nm.

5. Conclusions

In kainite and its Zn-analogue four structurally different Zn-sites (every in four different orientations) exist where Cu^{2+} can replace host zinc ion. We found that only one site is preferred for Cu^{2+} occupation. In this site Cu^{2+} is coordinated by four water molecules and two SO_4 groups. The other not occupied or weakly occupied sites have octahedral coordination with four SO_4 groups and two water molecules. Thus, during the crystal growth from a water solution a built up of Cu^{2+} complexes having four H_2O is preferred. Cu^{2+} substituting Zn^{2+} strongly deforms host lattice environment with an elongation of the coordination octahedron along SO_4–Cu–SO_4 direction (z-axis) and with rhombic distortion in the perpendicular plane as it is expected for strong Jahn–Teller effect. It is responsible for the strong g-factor anisotropy. The mixing of the $d_{x^2-y^2}$ and d_{z^2} in the ground state as well as the spin density delocalization *via* excited orbital states d_{xz} and d_{yz} have dominant influence on the spin-Hamiltonian parameter values. The mixing, although small, significantly shifts the g-factors and additionally reverses g-factor sequence. A relatively strong delocalization (up to about 30%) *via* exited antibonding orbitals is allowed by close and asymmetric location of Cl^- ions with respect to the Cu^{2+} complex.

One can expect, that thermally excited reorientations of the complex will involve a rotation around the z-axis, i.e., in-plane jumps of water molecules between x and y directions. We have found however, that this is not so. Instead of this the three potential wells of different energy are formed along the x, y, and z directions of Cu^{2+} complex. At low temperatures (below 20 K) all Cu^{2+} complexes are localized in the deepest potential well. Thermally excited jumps appear between two lowest energy wells only, i.e., the complex reorients between z and x directions. This is a typical behavior for the dynamic Jahn–Teller effect in Cu^{2+} complexes. We have found that the population of the higher energy well at low temperatures is smaller than that predicted by the Boltzmann statistic. Boltzmann population is reached when thermal energy becomes comparable with energy of the first exited vibrational level allowing effective inter-well tunneling. For this reason the widely user Silver–Getz model of inter-well's jumps is valid for high temperatures only. In low temperature range the classical model of motional averaging based on modified Bloch equation gives better results, since it works for any dynamical population of the higher energy well.

Pulsed EPR measurements confirmed that ESEEM spectroscopy is a strong method for an analysis of local environment of a paramagnetic center. Dipolar splitting observed in ESEEM spectrum confirmed our assignment of Cu^{2+} localization in the $KZnClSO_4{\cdot}3H_2O$ unit cell.

References

[1] P. Subramanian, N. Hariharan, Electron paramagnetic resonance study of Mn^{2+} in kainite, Pramana 26 (1986) 555–560.
[2] S. Dhanuskodi, A.P. Jeyakumari, EPR studies of VO^{2+} ions in kainite single crystal, Spectrochim. Acta A 57 (2001) 971–975.

[3] S.N. Rao, S. Vedanand, R. Ravikumar, R.V.S.S.N. Ravikumar, Y.P. Reddy, Optical absorption spectra of cobalt and nickel doped kainite, Solid State Commun. 92 (1994) 815–819.
[4] S.N. Rao, S. Vedanand, Y.P. Reddy, Spectroscopic investigations on vanadyl doped kainite, Sol State Commun. 73 (1990) 665–668.
[5] S. Dhanuskodi, N. Hariharan, ESR of Cu^{2+} in kainite, Cryst. Latt. Def. Amorph. Mater. 11 (1986) 361–367.
[6] B.D.P. Raju, N.O. Gopal, K.V. Narasimhulu, C.S. Sunandana, J.L. Rao, Variable temperature EPR spectra of copper(II) ions in kainite crystals, J. Phys. Chem. Solid 66 (2005) 753–761.
[7] S.C. Gedam, S.J. Dhoble, S.V. Moharil, Dy^{3+} and Mn^{2+} in $KMgSO_4Cl$ phosphor, J. Lumin. 124 (2007) 120–126.
[8] B.D.P. Raju, J.L. Rao, K.V. Narasimhulu, EPR and optical absorption studies on Cr^{3+} ions doped in $KZnClSO_4$ $3H_2O$ single crystal, Spectrochim. Acta A 61 (2005) 2195–2198.
[9] K.V. Narasimhulu, C.S. Sunandana, J.L. Rao, Spectroscopic studies of Cu^{2+} ions doped in $KZnClSO_4{\cdot}3H_2O$ crystals, Phys. Status Solid (a) 217 (2000) 991–997.
[10] K.V. Narasimhulu, C.S. Sunandana, J.L. Rao, Electron paramagnetic resonance studies of Cu^{2+} ions in $KZnClSO_4$ $3H_2O$: an observation of Jahn–Teller distortion, J. Phys. Chem. Solid 61 (2000) 1209–1215.
[11] P.D. Robinson, J.H. Fang, Y. Ohya, The crystal structure of kainite, Am. Mineral. 57 (1972) 1325–1332.
[12] M.A. Hitchman, C.D. Olson, R.L. Belford, Behavior of the in-plane *g*-tensor in low-symmetry d^1 and d^9 systems with application to copper and vanadyl chelates, J. Chem. Phys. 50 (1969) 1195–1203.
[13] D. Attanasio, ESR study of bis(ω-nitroacetophenonato)bis(4-methylpyridine)Cu(II): a six-coordinated low-symmetry copper chelate, J. Magn. Res. 26 (1977) 81–91.
[14] S.K. Hoffmann, J. Goslar, L.S. Szczepaniak, Low-symmetry doped Cu(II) complexes in $(gly)_2CaCl_2$ $4H_2O$ single crystal: EPR studies, Phys. Status Solid (b) 133 (1986) 321–328.
[15] J.D. Currin, Theory of exchange relaxation of hyperfine structure in electron spin resonance, Phys. Rev. 126 (1962) 1995–2001.
[16] B.L. Bales, D. Willett, EPR investigation of the intermediate spin exchange regime, J. Chem. Phys. 80 (1984) 2997–3004.
[17] A. Carrington, A.D. McLachlan, Introduction to Magnetic Resonance, Wiley, New York, 1979 (Chapter 12).
[18] W. Hilczer, S.K. Hoffmann, The pressure dependence of weak exchange coupling in $[Cu_2(dien)_2Cl_2](ClO_4)_2$ determined from single-crystal EPR measurements, Chem. Phys. Lett. 144 (1988) 199–202.
[19] S.K. Hoffmann, M. Krupski, W. Hilczer, High-pressure EPR studies of intermolecular interactions in solids, Appl. Magn. Res. 5 (1993) 407–427.
[20] R. Pirc, B. Zeks, P. Gosa, Kinetics of the alignment of O_2^- centers in stressed alkali halide crystals, J. Phys. Chem. Solid 27 (1966) 1219–1226.
[21] J.A. Sussmann, Quantum mechanical theory of barrier crossing by ions in solids, J. Phys. Chem. Solid 28 (1967) 1643–1648.
[22] V.S. Vikhnin, Orientational relaxation and spin–lattice relaxation due to tunneling controlled process, Fiz. Tverd. Tela 20 (1978) 1340–1346 (Russian).
[23] B.L. Silver, D. Getz, ESR of $Cu^{2+}(H_2O)_6$. II. A quantitative study of the dynamic Jahn–Teller effect in copper-doped zinc Tutton's salt, J. Chem. Phys. 61 (1974) 638–650.
[24] M.J. Riley, M.A. Hitchman, A.W. Mohammed, Interpretation of the temperature dependent *g*-values of the $Cu^{2+}(H_2O)_6$ ion in several host lattices using a dynamic vibronic coupling model, J. Chem. Phys. 87 (1987) 3766–3778.
[25] M. Marciniak, S.K. Hoffmann, M.A. Augustyniak, W. Hilczer, Comparative EPR studies of dynamics and exchange coupling in ammonium and potassium copper(II) Tutton salts, Phys. Status Solid (B) 191 (1995) 201–215.
[26] M.A. Augustyniak, A.E. Usachev, The host lattice influence on the Jahn–Teller effect of the $Cu(H_2O)_6^{2+}$ complex studied by EPR in $K_2Zn(SO_4)_2$ $6H_2O$ and $(NH_4)_2Zn(SO_4)_2$ $6H_2O$ Tutton salt crystals, J. Phys.: Condens. Matter 11 (1999) 4391–4400.
[27] S. Kiczka, S.K. Hoffmann, J. Goslar, L. Szczepanska, Electronic structure, Jahn–Teller dynamics and electron spin relaxation of two types of octahedral Cu(II) complexes in cadmium formate dehydrate. EPR and ESE studies, Phys. Chem. Chem. Phys. 6 (2004) 64–71.
[28] S.K. Hoffmann, J. Goslar, W. Hilczer, M.A. Augustyniak, M. Marciniak, Vibronic behavior and electron spin relaxation of Jahn–Teller complex $Cu(H_2O)_6^{2+}$ in $(NH_4)_2Mg(SO_4)_2$ $6H_2O$ single crystal, J. Phys. Chem. A 102 (1998) 1697–1707.
[29] S.K. Hoffmann, J. Goslar, W. Hilczer, M.A. Augustyniak-Jablokow, Electron spin relaxation of vibronic $Cu(H_2O)_6$ complexes in $K_2Zn(SO_4)_2$ $6H_2O$ single crystal, J. Phys.: Condens. Matter 13 (2001) 707–718.
[30] S. Idziak, J. Goslar, S.K. Hoffmann, Vibronic dynamics and electron spin relaxation of $Cu(formate)_4(H_2O)_2$ complexes in dibarium zinc formate tetrahydrate, $Ba_2Zn(HCOO)_6$ $4H_2O$ single crystal, Mol. Phys. 102 (2004) 55–61.
[31] S.S. Eaton, G.R. Eaton, Relaxation times of organic radicals and transition metal ions, in: L.J. Berliner, S.S. Eaton, G.R. Eaton (Eds.), Biological Magnetic Resonance, Distance Measurements in Biological Systems by EPR, vol. 19, Kluwer, New York, 2000, pp. 29–154.
[32] S. Lijewski, J. Goslar, S.K. Hoffmann, Electron spin echo of Cu^{2+} in the triglycine sulfate crystal family (TGS, TGSe, TGFB): electron spin–lattice relaxation, Debye temperature and spin–phonon coupling, J. Phys.: Condens. Matter 18 (2006) 6159–6169.
[33] S.K. Hoffmann, W. Hilczer, J. Goslar, EPR, electron spin–lattice relaxation, and Debye temperature of Cu(II)-doped triglycine selenate crystal, J. Magn. Res. 122 (1996) 37–41.
[34] K.M. Salikhov, A.G. Semenov, Yu.D. Tsvetkov, Electron Spin Echoes and Their Applications, Nauka, Novosibirsk, 1976 (Russian).
[35] S.K. Hoffmann, J. Goslar, W. Hilczer, M.A. Augustyniak-Jablokow, S. Kiczka, Dephasing relaxation of the electron spin echo of the vibronic $Cu(H_2O)_6$ complexes in Tutton salt crystals at low temperatures, J. Magn. Res. 153 (2001) 56–68.
[36] K.M. Salikhov, S.A. Dzuba, A.M. Raitsimring, The theory of electron spin echo signal decay resulting from dipole–dipole interaction between paramagnetic centers in solids, J. Magn. Res. 42 (1981) 255–276.